Fabrication and Evaluation of Nanoelectrode Ensembles

Vinod P. Menon and Charles R. Martin*
Department of Chemistry
Colorado State University
Fort Collins, CO 80523

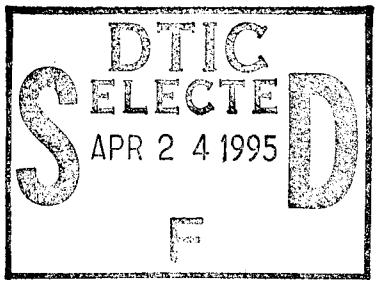

*Corresponding author

ABSTRACT

An electroless deposition procedure for filling the pores in nanoporous filtration membranes with metal (gold) nanowires is described. This method allows us to routinely prepare ensembles of gold nanodisk electrodes in which the nanodisks have diameters as small as 10 nm. Results of electrochemical experiments at ensembles of 30 nm-diameter and 10 nm-diameter gold-disk electrodes are described. The electrochemical response characteristics of these nanoelectrode ensembles are in agreement with predictions of the relevant electrochemical theories. Cyclic voltammetric detection limits for electroactive species at ensembles containing 10 nm-diameter gold disks can be as much 3 orders of magnitude lower than at a large-diameter gold-disk electrode.

REPORT DOCUMENTATION PAGE

OMB No. 0704-0188

1. AGENCY USE ONLY (Leave blank)	2. REPORT DATE	3. REPORT TYPE AND DATES COVERED
	4/18/ 1995	Interim

4. TITLE AND SUBTITLE
Fabrication and Evaluation of Nanoelectrode Ensembles

5. FUNDING NUMBERS
Contract
N00014-82K-0612

6. AUTHOR(S)
Vinod P. Menon and Charles R. Martin

7. PERFORMING ORGANIZATION NAME(S) AND ADDRESS(ES)
Dr. Charles R. Martin
Department of Chemistry
Colorado State University
Fort Collins, CO 80523

8. PERFORMING ORGANIZATION REPORT NUMBER
ONR TECHNICAL REPORT #102

9. SPONSORING / MONITORING AGENCY NAME(S) AND ADDRESS(ES)
Office of Naval Research
800 North Quincy Street
Arlington, VA 22217

10. SPONSORING / MONITORING AGENCY REPORT NUMBER

11. SUPPLEMENTARY NOTES

12a. DISTRIBUTION / AVAILABILITY STATEMENT
Reproduction in whole or part is permitted for any purpose of the United States Government. This document has been approved for public release and sale; its distribution is unlimited.

12b. DISTRIBUTION CODE

13. ABSTRACT *(Maximum 200 words)*

An electroless deposition procedure for filling the pores in nanoporous filtration membranes with metal (gold) nanowires is described. This method allows us to routinely prepare ensembles of gold nanodisk electrodes in which the nanodisks have diameters as small as 10 nm. Results of electrochemical experiments at ensembles of 30 nm-diameter and 10 nm-diameter gold-disk electrodes are described. The electrochemical response characteristics of these nanoelectrode ensembles are in agreement with predictions of the relevant electrochemical theories. Cyclic voltammetric detection limits for electroactive species at ensembles containing 10 nm-diameter gold disks can be as much as 3 orders of magnitude lower than at a large-diameter gold-disk electrode.

14. SUBJECT TERMS	15. NUMBER OF PAGES
Nanoelectrodes, ultramicroelectrodes, electrochemistry nanometals	16. PRICE CODE

17. SECURITY CLASSIFICATION OF REPORT	18. SECURITY CLASSIFICATION OF THIS PAGE	19. SECURITY CLASSIFICATION OF ABSTRACT	20. LIMITATION OF ABSTRACT
		UNCLASSIFIED	

OFFICE OF NAVAL RESEARCH

Contract N00014-82K-0612

R&T CODE: 4133032
Robert J. Nowak

TECHNICAL REPORT NO. 102

Fabrication and Evaluation of Nanoelectrode Ensembles

by

Vinod P. Menon and Charles R. Martin

Prepared for publication

in

Analytical Chemistry

Department of Chemistry
Colorado State University
Ft. Collins, CO 80523

April 18, 1995

INTRODUCTION

Electrochemistry at electrodes with microscopic dimensions constitutes one of the most important frontiers in modern electrochemical science (1). Such electrodes offer a myriad of opportunities including the possibility of doing electrochemistry in highly resistive media (2-4) and the possibility of investigating the kinetics of redox processes that are too fast to study at electrodes of conventional dimensions (5-9). Numerous methods for preparing microscopic electrodes have been devised (10), and it is now fairly easy to make electrodes with dimensions on the order of microns (e.g. a 5 μm-diameter metal disk) (8).

While White's group has developed a method for preparing band electrodes with nanoscopic band widths (11), making nanoscopic disk-shaped electrodes (e.g. diameters less than 100 nm) has proven to be a much more elusive goal (12-14). This is, however, an extremely important goal because theory predicts that such truly nanoscopic electrodes could be useful for studying the kinetics of ultrafast electron transfer reactions (15). In addition, interesting and unusual electrochemical phenomena have been predicted to occur at such nanoscopic electrodes (16). Hence, this is an area of science where theory is ahead of experimental practice due to the difficulties in preparing truly nanoscopic electrodes.

We have previously shown that the pores in microporous filtration membranes can be used as templates for the preparation of ensembles of microdisk electrodes (17-19). The membranes employed contain cylindrical pores with uniform diameters. We electrochemically deposited metal microwires within these pores; the ends of these microwires (at one face of the membrane) defined the microscopic disk-shaped electrodes . Unfortunately, the smallest electrodes we could achieve using electrochemical deposition of metal within the pores of such membranes had diameters on the order of 200 nm (17).

In this report we introduce a new electroless deposition procedure for filling the pores of such membranes with metal (gold) nanowires. This electroless deposition chemistry allows us to routinely prepare ensembles of gold nanodisk electrodes in which the nanodisks have diameters as small as 10 nm. We describe the results of electrochemical experiments at ensembles of 30 nm-diameter and 10 nm-diameter gold-disk electrodes. We show via comparisons of experimental and simulated cyclic voltammograms, and through other experimental data, that the electrochemical response characteristics of these new nanoelectrode ensembles (NEEs) are in agreement with predictions of the relevant electrochemical theories. We also show that cyclic voltammetric detection limits for electroactive species (19) at ensembles containing 10 nm-diameter gold disks can be as much 3 orders of magnitude lower than at a large-diameter (3.17 mm) gold disk electrode.

EXPERIMENTAL

Materials. Anhydrous $SnCl_2$ (Aldrich), $AgNO_3$ (Spectrum), trifluoroacetic acid, Na_2SO_3, NH_4OH, formaldehyde, anhydrous methanol and concentrated HNO_3 (Mallinckrodt) were used as received. Commercial gold electroless plating solution (Oromerse Part B, Technic Inc.) was diluted (40 times with water) prior to use. Milli Q 18-MΩ water was used for rinsing and for all solutions. $NaNO_3$ (Mallinckrodt) and $Ru(NH_3)_6Cl_3$ (Strem) were recrystallized prior to use. Trimethylaminomethylferrocene ($TMAFc^+$) perchlorate was prepared by metathesis from the iodide salt (20) and recrystallized. The iodide salt was prepared from dimethylaminomethylferrocene (Aldrich) according to the established procedure (21). $K_4[Mo(CN)_8]$ was synthesized according to the established procedure and purified (22).

"Track-etch" (23) polycarbonate membrane filters were obtained from Poretics. Filters with pore diameters of 10 nm and 30 nm were used to make the

nanoelectrode ensembles (NEEs). The pore densities and average center-to-center distances between pores for these membranes are shown in Table I. Multiplying the pore density (pores/cm^2) by the cross-sectional area of a single pore (cm^2/pore), provides a parameter called the fractional pore area (17-19,24,25) (Table I). This is an important parameter because, assuming that each pore produces an active nanodisk electrode, the fractional pore area is equivalent to the fractional electrode area, which is the sum of the areas of the Au-nanodisk elements in the NEE divided by the geometric area of the NEE. We have shown that the fractional electrode area can be determined experimentally from the double layer charging currents obtained at the NEE (17-19). Ideally, this experimental fractional electrode area and the fractional pore area should be equivalent (Table I). Finally, these membranes have a "rough" and a "smooth" face (19). The rough face has a dull (i.e. non-shiny) appearance.

Electrochemical and other measurements. Cyclic voltammetry was used to explore both the faradaic and double-layer charging currents at the NEEs. Electrochemical measurements were made with a PAR Model 273 potentiostat in conjunction with a PAR Model 175 programmer and a Soltec Model VP6424S X-Y recorder or a Nicolet Model 310 digital storage oscilloscope. Ninety percent iR-compensation was employed for all measurements (17). All solutions were purged with nitrogen prior to use. Scanning electron micrographs were obtained on a Philips 505 microscope. Transmission electron micrographs were obtained on a JEOL 2000. Digital simulations were carried out using DIGISIM (BAS Inc.), a cyclic voltammetric simulations program, running on an Applied Computer Technology, Model 486/66-520 E/S computer.

Electroless deposition. Electroless metal deposition involves the use of a chemical reducing agent to plate a metal from solution onto a surface (26). The advantage of the electroless method (relative to electrochemical plating) is that

the surface to be coated need not be electronically conductive. The key requirement of an electroless deposition bath of this type is to arrange the chemistry such that the kinetics of homogeneous electron transfer from the reducing agent to the metal ion are slow. This is essential because otherwise the metal ion would simply be reduced in the bulk solution. A catalyst that accelerates the rate of metal ion reduction is then applied to the surface to be coated. In this way, metal ion is reduced only at the surface, and the surface becomes coated with the desired metal.

The electroless deposition chemistry used here is shown schematically in Figure 1. Prior art in the electroless deposition field (27) was very useful in developing this chemistry; however, we have made significant modifications in the prior art in order to make this process compatible with the membrane chemistry and with the objective of plating gold uniformly in nanoscopic pores. A "sensitizer" (Sn^{2+}) was first applied to the surfaces (pore walls plus faces) of the membrane. This was accomplished by simply immersing the membrane into a solution that was 0.026 M in $SnCl_2$ and 0.07 M in trifluoroacetic acid; the solvent was 50/50 methanol/water . The membrane was immersed into this solution for three minutes. The membrane was then rinsed with three 100 mL portions of methanol. Sn^{2+} adheres to the pore walls (Figure 1A) and membrane faces because the membrane is coated with a layer of polyvinylpyrrolidone (PVP) during production. This is done in order to render the membranes hydrophilic. PVP contains metal-ion-complexing amine and carbonyl groups. We believe that these groups act as "molecular anchors" (28) that bond the Sn^{2+} to the surfaces of the membrane (Figure 1A).

The Sn^{2+}-sensitized membrane was then activated by immersion into an aqueous solution of ammoniacal $AgNO_3$ (0.029 M) (29) for two minutes. This

causes a redox reaction in which the surface-bound Sn(II) gets oxidized to Sn(IV) and the Ag^+ gets reduced to elemental Ag; some silver oxide is also obtained (30). As a result, the pore walls and membrane faces become coated with discrete, nanoscopic Ag particles (Figure 1B). After Ag deposition, the membrane was rinsed in two 100 mL portions of methanol and then immersed into water. These processes of Sn(II) activation followed by reduction of Ag(I) to Ag(0) have been studied in detail on glass surfaces (27).

The Ag-coated membrane was then immersed into an Au plating bath that was 7.9×10^{-3} M in $Na_3Au(SO_3)_2$ (the diluted form of the commercial plating solution), 0.127 M in Na_2SO_3, and 0.625 M in formaldehyde; the temperature of this bath was ca. 2° C. The Ag particles are galvanically displaced by Au since gold is a more noble metal. As a result, the pore walls and faces become coated with Au particles (Figure 1C). These particles are excellent catalytic sites for the oxidation of formaldehyde and the concurrent reduction of Au(I) to Au°. As a result, gold plating continues on the gold particles, using formaldehyde as the reducing agent. This reaction can be represented as follows:

$$2Au(I) + HCHO + 3OH^- \text{ ----------> } HCOO^- + 2H_2O + 2\,Au \qquad (1)$$

Au plating was continued for a period of 24 h, resulting in the deposition of Au nanowires (see below) into the pores. In addition, both faces of the membrane become coated with thin (ca. 500 nm-thick) Au films. We refer to this membrane that has Au films on both faces and Au nanowires running through the pores as the Au/Au-PC/Au membrane, where Au-PC stands for the Au-nanowire-containing polycarbonate. After plating, the Au/Au-PC/Au membrane was thoroughly rinsed with water and then immersed in 25% nitric acid for 12 h. This was done to dissolve any residual Sn or Ag that might be left in the membrane. The membrane was then rinsed thoroughly in water and air-dried.

NEE Fabrication. The NEE fabrication procedure is shown schematically in Figure 2. A 5 mm x 6 mm piece of the Au/Au-PC/Au membrane is first affixed to a 6 mm x 15 mm piece of adhesive aluminum foil tape (All-Foils Inc.) (Figure 2A). The Au/Au-PC/Au membrane is placed on the Al foil tape such that the Au film covering the rough face (see above) of the membrane is down (i.e. against the adhesive). A rectangular strip (6 mm x 40 mm) of a copper foil, with a conductive adhesive (3M Scotch brand electrical tape #1739-7), is then affixed to the upper Au-coated surface of the Au/Au-PC/Au membrane. (The adhesive is conductive because it contains Ni particles.) The copper foil is positioned such that it covers only about 1 mm of the 6 mm length of the Au/Au-PC/Au membrane (Figure 2B).

This Cu foil-tape acts as a current collector and working electrode lead for the NEE. The upper Au surface layer from the portion of the Au/Au-PC/Au membrane not covered by the Cu foil-tape is then removed by simply applying and then removing a strip of Scotch tape (3M Scotch brand Magic tape #810) (Figure 2C). Removal of the Au surface layer exposes the disk-shaped ends of the Au nanowires within the pores of the membrane (Figure 2C). These nanodisks will become the active electrode elements.

At this point, the NEE assembly is heat-treated at 150° C for 15 min. As will be discussed in detail below, this produces a water-tight seal between the Au nanowires and the pore walls. Finally, strips of strapping tape (3M Scotch brand # 898) are applied to the lower and upper surfaces of the assembly to insulate the Al and Cu-foil tapes (Figure 2D). A 0.079 cm^2 hole is punched into the upper piece of tape prior to placement on the assembly. This hole defines the area of the NEE that is exposed to the solution. We refer to this area as the geometric area of the NEE. The active electrode area of the NEE is this geometric area multiplied by the fractional electrode area (Table I) (17-19). The electrochemical response at the NEEs was compared to that of a "macroscopic" Au-disk

electrode that had an active area equivalent to the geometric area of the NEE, 0.079 cm^2. This gold macro-disk electrode was obtained from BAS Inc.

Optical characterization of the NEEs. Nanometals have interesting and characteristic optical properties (31,32). Optical absorption spectra of the Au nanowire-containing membranes were obtained by removing both of the Au surface layers from the Au/Au-PC/Au membranes. A piece of the resulting Au-PC membrane was then placed in the beam of a Hitachi U-3501 UV/visible/near-IR spectrophotometer, and a conventional transmittance spectrum of the membrane was obtained (31,32).

RESULTS AND DISCUSSION

Au Deposition and NEE Fabrication. The key feature of the electroless deposition process is that Au deposition begins at the pore wall. As a result, after brief deposition times, a hollow Au tubule is obtained within each pore (33). These tubules can be imaged by taking transmission electron micrographs of microtomed sections of the tubule-containing membrane. An image of this type for a membrane that contained 50 nm-diameter pores is shown in Figure 3A. The Au tubules (black rings) appear elliptical (and ragged) due to distortion by the microtoming process.

Scanning electron microscopy can be used to image the surface of the membrane after removal of the Au surface layer. An image of this type for a membrane that contained 30 nm-diameter pores is shown in Figure 3B. Nearly circular Au disks with diameters of ca. 30 nm are observed at the surface. Ideally all of the pores should make an angle of 90° with the membrane surface. In fact, however, pores that vary by as much as $\pm$34° from surface normal are obtained. Since electrons are capable of penetrating through some finite thickness of the polycarbonate membrane, small portions of the Au nanowires in the angled tracks are visible in the electron micrograph. This is responsible for the streaks

observed in the micrograph (Figure 3B). Counting the number of nanodisks observed in such images allows for an experimental evaluation of the pore density. We have found that the pore densities for these membranes are, within experimental error, identical to the values supplied by the manufacturer (Table I).

Finally, dissolving away the polycarbonate template membrane in dichloromethane (17) (after removing both Au surface layers) allows us to view the Au nanowires that extend through the membrane thickness. Figure 3C shows a scanning electron micrograph of nanowires grown in a 50 nm pore-diameter membrane. As expected, these nanowires are ca. 6μm in length (the thickness of the membrane).

As indicated in Figure 2, the NEEs were fabricated by applying the bottom surface of the Au/Au-PC/Au membrane to Al-foil tape and then applying a Cu-foil tape with a conductive adhesive to the upper surface of the membrane. The alternative would be to simply apply the Cu foil-tape to the bottom of the Au/Au-PC/Au membrane and thus eliminate the need for the Al-foil tape. The adhesive used for the Cu foil is conductive because it contains Ni particles. When this foil was applied directly to the bottom of the Au/Au-PC/Au membrane, the Ni particles often punctured the membrane. Applying the Al-foil tape to the bottom of the Au/Au-PC/Au membrane, and then making electrical contact from the top with the Cu-foil tape, prevents punctures in the region of the membrane that is exposed to the solution (Figure 2).

Optical Properties of the NEEs. Nanometals have interesting optical properties. For example, suspensions of nanoscopic Au particles can be pink, purple or blue depending on the diameter of particles (34). These colors arise from the plasmon resonance absorption of the nanometal particle, a phenomenon we have explored in some detail (31,32). We have shown that membranes containing Au nanowires like those described here also show this plasmon

resonance band, and as a result, such membranes can show a wide variety of colors (31,32,35). This absorption in the visible region provides an interesting optical approach for characterizing the Au nanowire-containing membranes.

Figure 4 compares absorption spectra for membranes containing 10 nm-diameter and 30 nm-diameter Au nanowires. Note that the wavelength of maximum absorption intensity for the membrane containing the 10 nm-diameter nanowires is blueshifted relative to that for the membrane containing the 30 nm-diameter nanowires. This blueshift for the smaller diameter nanowires is in qualitative agreement with the predictions of effective medium theory (31,32). As would be expected from the spectra shown in Figure 4, the membranes containing the 10 nm-diameter nanowires appear pink in color whereas the membranes containing the 30 nm-diameter nanowires are purple. Because of these distinctive colors it is easy to distinguish the 30 nm disk-diameter NEEs (30NEEs) from the 10 nm disk-diameter NEEs (10NEEs).

Double-layer charging currents. A persistent problem with micro and nanoelectrodes is the sealing of the conductive element to the insulating material that surrounds the element such that solution does not creep into this junction (17,36). This solution creeping is undesirable because it causes the double layer charging currents to be spuriously large (17,36). Previous methods for improving the seal have included silanization of the surrounding insulator (36) and impregnating the junction between the electrode and the insulating material with low molecular weight polyethylene (17). However, neither of these methods have proven completely satisfactory. In this report we introduce a superior method for sealing the junction between the Au nanowires and the polycarbonate host membrane. This method exploits the heat-shrinkability of the template membrane.

The polycarbonate membranes are stretch-oriented during fabrication in order to improve their mechanical properties. If the membrane is subsequently heated above its glass-transition temperature (ca. 150° C), the polymer chains relax to their unstretched conformation, and the membrane shrinks. This shrinking of the membrane around the Au nanowires in the pores causes the junction between the nanowire and the pore wall to be sealed. This is illustrated in Figure 5, which shows voltammograms for $TMAFc^+$ before (Figure 5A) and after (Figure 5B) the heat-treatment procedure. Before heat treatment, the double layer charging currents are pronounced. In contrast, after heat treatment, the charging currents are not discernible at the current-sensitivity setting used.

We have used voltammetric measurements in the absence of the electroactive species to quantitatively evaluate this new heat-sealing procedure. The magnitude of the double layer-charging current can be obtained from these voltammograms (17-19), and this allows for a determination of the fractional electrode area (Table I). This experimental fractional electrode area can then be compared to the fractional pore area calculated from the known pore diameter and density of the membrane (Table I). In order to use this method, the double layer capacitance of the metal must be known (17-19). The double layer capacitance of Au was determined from measurements of charging currents at Au macro-disks electrodes of known area (Figure 6, curve a) . A value of 21 $\mu F\ cm^{-2}$ was obtained.

Figure 6 compares double layer charging currents obtained at a 10NEE, a 30NEE, and an Au macro-disk electrode with active area equal to the geometric areas of the NEEs. As would be expected the charging currents at the NEEs are significantly lower than at the macro-disk electrode. The fractional electrode areas obtained from the double layer charging currents at the NEEs are shown in Table I. The fractional electrode area for the 30NEE is, within experimental error,

identical to the fractional pore area (Table I). This indicates that all pores are filled with Au and that the heat-shrinking procedure used to seal the 30 nm-diameter Au nanowires that run through the membrane is quite effective.

The fractional electrode area at the 10NEE is within a factor of two of the fractional pore area. This larger-than-expected fractional electrode area may result from a small amount of solution leakage around the 10 nm-diameter Au nanowires. The alternative possibility is that the pore density and/or pore size determined by electron microscopy is slightly off. This is a likely possibility because it is difficult to image 10 nm structures using scanning electron microscopy. Given the general observation that the sealing problem for a micro or nanoelectrode becomes worse as the diameter of the electrode decreases (17,36), the agreement between the fractional electrode areas and the fractional pore areas (Table I) is satisfactory.

Faradaic Currents. The nature of the faradaic currents observed at a NEE depend on the distance between the electrode elements and the time scale (i.e. scan rate) of the experiment (17-19,24). The NEEs used here will be in the "total-overlap" (17-19,24) response regime, at any scan rate below ca. 2800 V s^{-1} (see Appendix A). In this total-overlap regime, the diffusion layers at the individual elements of the NEE have overlapped to produce a diffusion layer that is linear to the entire geometric area of the NEE (17-19,24). As a result, conventional peaked-shaped voltammograms are obtained. Indeed, for the reversible case, the voltammogram at a NEE operating in this total-overlap regime should be identical to the voltammogram obtained at a macro-disk electrode with active area equivalent to the geometric area of the NEE (17-19,24).

Experimental and simulated cyclic voltammograms for a solution that was 5 μM in $TMAFc^+$ and 0.5 mM in supporting electrolyte (sodium nitrate) are shown

in Figure 7. The experimental data were obtained at a 10NEE. In agreement with the above discussion, the experimental voltammograms are peak shaped and peak current increases with the square root of scan rate. This latter point is proven by the agreement between the experimental and simulated voltammograms. The simulated data were obtained by assuming reversible electrochemistry at a macro-disk electrode with active area equivalent to the geometric area of the NEE. Other than assuming an arbitrarily high value for the standard heterogeneous rate constant, there are no adjustable parameters in these simulations. The quantitative agreement between the experimental and simulated voltammograms indicates that the reversible, total-overlap limiting case is, indeed, operative at the NEE.

Three other comments are worth making regarding the data in Figure 7. First, the concentration of both the electroactive species (5 μM) and the supporting electrolyte (0.5 mM) are low. Low concentrations were used because we have discovered an interesting effect of supporting electrolyte concentration on the electrochemistry observed at the NEEs; the reversibility of the voltammetric waves for all couples investigated to date ($TMAFc^{+/2+}$, $Ru(NH_3)_6^{3+/2+}$, $Mo(CN)_8^{4-/3-}$) improves as the concentration of supporting electrolyte decreases (see below). This is why low concentrations of supporting electrolyte (and correspondingly low concentrations of electroactive species) were used here.

Second, it is possible that such low supporting electrolyte concentrations exacerbate problems of uncompensated solution resistance. At the concentration of electroactive species and the scan rates used here, the current at the NEEs are low (e.g. less than 100 nA in Figure 7). As a result, uncompensated solution resistance distorts the voltammograms to a negligible extent, even at the mM supporting electrolyte concentrations used here. Indeed,

voltammograms with and without application of 90% iR compensation are identical.

Third, the experimental voltammograms in Figure 7 have not been corrected for background currents. Nevertheless, the agreement between the experimental and simulated voltammograms (where only faradaic currents are simulated) is good. Background subtraction is not necessary, at these scan rates, because the double layer charging currents at the NEEs are orders of magnitude lower than at a macro-electrode of equivalent geometric area (Figure 6). Because the faradaic currents at the NEE and the macro-electrode are, for the reversible case, identical (Figure 7), this diminution in the background currents also means the signal-to-background ratio (14,19) at the NEE is orders of magnitude larger than at the macro-electrode. This point will be explored further below. It is this enhancement in signal-to-background ratio that allows us to use such low concentrations of electroactive species.

So far we have discussed only the reversible case. The equivalence of the net faradaic current at the NEE and at a macro-electrode of the same geometric area (Figure 7) means that the flux at the individual elements of the NEE are many orders of magnitude larger than the flux at the macro-electrode. Indeed, the experimentally-determined fractional electrode areas (Table I) indicate that, for the reversible case, the flux at the elements of a 10-NEE will be ca. 1000 times higher than at the macro-electrode; the flux at the elements of the 30NEE will be ca. 250 times higher. The higher fluxes at the NEE elements means that the NEEs will be more sensitive to the kinetics of electron transfer than a macro-electrode (14,15).

The simplest way to think about this situation is that for any redox couple, the quasireversible case can be observed at a NEE at much lower scan rates than at a macro-electrode (14). Indeed, because flux is related to the square root

of scan rate, the 10^3-fold enhancement in flux at the 10NEE means that one would have to scan a macro-electrode at a scan rate 10^6 times higher in order to obtain the same kinetic information obtainable at the NEE. That is, if for a particular redox couple one observed quasireversible voltammetry at the 10NEE at scan rates above 1 V s^{-1}, one would have to scan at rates above 10^6 V s^{-1} to achieve the quasireversible case for this couple at a macro-electrode. This ability to obtain kinetic information at dramatically lower scan rates is an important advantage of a NEE (14).

The $Ru(NH_3)_6^{3+/2+}$ voltammograms shown in Figure 8 illustrate this point. The standard heterogeneous rate constant for this couple has been measured by a number of groups (12,14,37); values of 0.26 (12) ,1.8 (14), and 76 (37) cm s^{-1} have been reported. Assuming, for the sake of illustration, a value of 1 cm s^{-1}, Nicholson's theory shows that quasireversible $Ru(NH_3)_6^{3+/2+}$ voltammograms will be obtained, at a macro-electrode, at scan rates above ca. 5 V s^{-1} (38) .

Figure 8A shows voltammograms at various scan rates for $Ru(NH_3)_6^{3+/2+}$ at a 30NEE. The peak separation (ΔE_{pk}) values are shown in Table II. This couple shows reversible voltammetry ($\Delta E_{pk} \approx 59$ mV) at the lowest scan rates shown, but the voltammograms become quasireversible at scan rates above 0.01 V s^{-1} (Table II). Therefore, as expected, the transition to quasireversible behavior is observed at dramatically lower scan rates at the 30NEE than would be observed at a macro-electrode. It is again important to emphasize that the increase in ΔE_{pk} observed in Table II is not due to uncompensated solution resistance .

Because the fractional electrode area at the 10NEE is lower than at the 30NEE (Table I), the transition to quasireversible behavior would be expected to occur at even lower scan rates at the 10NEE. Voltammograms for

$Ru(NH_3)_6^{3+/2+}$ at a 10NEE are shown in Figure 8B. The corresponding ΔE_{pk} values are shown in Table II. At the 10NEE it is impossible to obtain the reversible case, even at a scan rate as low as 5 mV s^{-1} (Table II). The effect of quasireversible electrochemistry is also clearly seen in the diminution of the voltammetric peak currents at the 10NEE (relative to the 30NEE). This diminution in peak current (relative to the reversible case) is characteristic of the quasireversible case at an ensemble of nanoelectrodes (14,24).

We will have more to say about the kinetics of electron transfer reactions at NEEs in a forth-coming paper (39). These preliminary studies indicate, however, that the response characteristics of the NEEs are in qualitative agreement with theoretical predictions (14,24).

Electroanalytical detection limits at the NEEs. For the reversible case, the voltammetric detection limit for a redox species at a NEE should be the detection limit for the same species at the corresponding macro-electrode multiplied by the fractional electrode area (Table I) of the NEE (19). Because the fractional electrode area for the 10NEE is ca. 10^{-3}, this suggests that the voltammetric detection limit at a 10NEE should be three orders of magnitude lower than the detection limit obtained at a macro-electrode. Figure 9A shows voltammograms at a macro-electrode at various low concentrations of $TMAFc^+$. As would be expected, the faradaic signal ultimately vanishes into the background double-layer-charging currents. Taking a total measured current that is twice the background charging current as the criterion for establishing the detection limit (19), these voltammograms show that the detection limit for $TMAFc^+$ at the macro-electrode is ca. 1.6 μM (see Figure 10A).

Voltammograms for various low concentrations of $TMAFc^+$ at a 10NEE are shown in Figure 9B. While the voltammograms look nearly identical to those obtained at the macro-electrode, the concentrations are three orders of

magnitude lower. Using the same criterion for the detection limit, we obtain a detection limit at the 10NEE that is three orders of magnitude lower (1.6 nM) than at the macro-electrode. This is illustrated by the calibration curve shown in Figure 10B. It is gratifying that the experimentally-observed enhancement in detection limit at the NEE is exactly as would be predicted from the fractional electrode area data in Table I.

Cyclic voltammetry is generally considered to be a poor electroanalytical technique. This is because the high double-layer charging currents observed at a macro-electrode make the signal-to-background ratio low. The voltammograms in Figure 9B, and the corresponding calibration curve for the 10-NEE in Figure 10B, clearly show that at the NEEs, cyclic voltammetry is a very powerful electroanalytical technique. There is, however, a caveat. Because the NEEs are more sensitive to electron transfer kinetics, the enhancement in detection limit that is in principle, possible, could be lost for couples with low values of the heterogeneous rate constant. This is because one effect of slow electron transfer kinetics at the NEE is to lower the measured faradaic currents (e.g. Figure 8) (14,24).

This sensitivity to slow electron transfer kinetics could however prove to be an advantage in sensor applications where a mediator, with fast electron transfer kinetics, is used to shuttle electrons to a redox enzyme (40). Chemical species that are electroactive in the same potential region as the mediator can act as interferants at such sensors. If such an interfering electroactive species shows slow electron transfer kinetics, it might be possible to eliminate this interference at the NEE. This is because at the NEE, the redox wave for the kinetically-slow interferant might be unobservable in the region where the kinetically-fast mediator is electroactive. We are currently exploring this possibility.

The Effect of Supporting Electrolyte. As indicated above, all of the experimental data reported thus far were obtained at low concentrations of both supporting electrolyte (≈ mM) and electroactive species (≈ μM). This was done because we have observed an interesting effect of supporting electrolyte concentration on the shape of the voltammetric waves observed at the NEEs. We have found that the reversibility of the voltammetric waves for all couples investigated to date ($TMAFc^{+/2+}$, $Ru(NH_3)_6^{3+/2+}$, $Mo(CN)_8^{4-/3-}$) improves as the concentration of supporting electrolyte decreases. This effect is illustrated, for $TMAFc^{+/2+}$ in Figure 11. Note that the peak currents decrease and the ΔE_{pk} values increase as the concentration of supporting electrolyte increases.

This effect has been observed in all of the supporting electrolytes we have investigated to date; these include $NaNO_3$, $NaClO_4$, Na_2SO_4, Et_4NBF_4, Et_4NClO_4, $Mg(NO_3)_2$, KNO_3, KPF_6, $ZnSO_4$, and pH = 7.0 phosphate buffer. Furthermore, this effect is reproducible and reversible. By reversible we mean that if the NEE is taken out of a solution with high supporting electrolyte concentration (e.g. 50 mM) and returned to a solution with low electrolyte concentration (e.g. 1 mM), the voltammetric wave immediately assumes the reversible appearance characteristic of the low electrolyte-concentration solution (Figure 11). Furthermore, we have observed this effect for NEEs prepared from both polycarbonate and polyester membranes, and we have observed it for NEEs prepared from membranes with and without the PVP that is used to improve membrane wettability.

This supporting electrolyte effect will be discussed in detail in a forthcoming paper, which will focus on using these NEEs to obtain standard heterogeneous rate constant data for fast redox couples (39).

CONCLUSIONS

We have described in this paper a new method for preparing electrodes with nanoscopic dimensions. We have used this method to prepare nanoelectrode ensembles with individual electrode-element diameters as small as 10 nm. This method is simple, inexpensive, and highly reproducible. The reproducibility of this approach for preparing nanoelectrodes is illustrated by the fact that NEEs given to other groups yielded the same general electrochemical results as obtained in our laboratory (41). These NEEs display cyclic voltammetric detection limits that are as much as three orders of magnitude lower than achievable at a conventional macro-electrode.

The electroless metal deposition procedure described here is general and can be extended to the deposition of a number of metals. It can also be modified to create interesting nanostructures such as metal nanotubules (33). Indeed, the methods developed here are a part of a much larger research effort in this laboratory aimed at using the pores in such nanoporous membranes as a general approach for preparing nanomaterials (35).

Acknowledgments. This work was supported by the Office of Naval Research. We acknowledge Ranjani V. Parthasarathy for help with scanning electron microscopy and Matsuhiko Nishizawa for help with transmission electron microscopy.

Appendix A. The scan rate below which total overlap occurs can be approximated as follows; see (19) for further discussion. The average center-to-center distance between disks in a random ensemble is given by one-half of the inverse square root of the disk density, or 204 nm for the NEEs studied here (Table I). The average edge-to-edge distance between disks is then 194 nm for the 10NEE and 174 nm for the 30NEE. We assume that the NEEs will go out of total overlap when the diffusion layer at an element extends less than half of the average edge to edge distance between elements; so, the 10NEE will go out of total overlap when the diffusion layer at the elements is on average less than ca. 100 nm in thickness.

Using the Einstein-Smoluchowski equation, $L = (2Dt)^{1/2}$, and substituting 100 nm in for L and 5.5×10^{-6} cm^2 s^{-1} for D, we find that the 10NEE will be in total overlap at $t > 9$ μs. The voltammetric scan rate equivalent to this t can be calculated using $\upsilon = RT/nFt$. This calculation shows that the 10NEE will be in total overlap at $\upsilon < 2850$ V s^{-1}. While this is a crude calculation, we use scan rates that are more than three orders of magnitude lower than this value. Hence, there is no question that the NEEs are in total overlap in the scan rate region used here. This is proven by the simulations shown in Figure 7.

REFERENCES

1. Montenegro, M. I.; Queiros, M. A.; Daschbach, J. L.; Eds.; *Microelectrodes: Theory and Applications.* NATO ASI Series, 1990, Series E: Applied Sciences, Dodrecht, The Netherlands, Vol 197.
2. Drew, S. M.; Wightman, R. M. *J. Electroanal. Chem.* **1991,** *317,* 117-124.
3. Bento, M. F.; Medeiros, M. J.; Montenegro, M. I.; Beriot, C.; Pletcher, D. *J. Electroanal. Chem.* **1993,** *345,* 273-286.
4. Reference 1, Section 3, pp. 177-189.
5. Russell, A.; Repka, K.; Dibble, T.; Ghoroghchian, J.; Smith, J.J.; Fleischmann, M.; Pitt, C.H.; Pons, S. *Anal. Chem.* **1986,** *58,* 2961-2964
6. Bond, A. M.; Henderson, T. L. E.; Mann, D. R.; Thormann, W.; Zoski, C. G. *Anal. Chem.* **1988,** *60,* 1878-1882.
7. Oyama, N.; Ohsaka, T.; Yamamoto, N.; Matsui, J.; Hatozaki, O. J. *Electroanal. Chem.* **1989,** *265,* 297-304.
8. Karpinski, Z. J.; Osteryoung, R. A. *J. Electroanal. Chem.* **1993,** *349,* 285-297.
9. Safford, L. K.; Weaver, M. J. *J. Electroanal. Chem.* **1992,** *331,* 857-876.
10. Reference 1, Section 4, pp. 189-227.
11. Morris, R. B.; Franta, D. J.; White, H. S. *J. Phys. Chem.* **1987,** *91,* 3559-3564.
12. Penner, R. M.; Heben, M. J.; Longin, T. L.; Lewis, N. S. *Science,* **1990,** *250,* 1118-1121.
13. Pendley, B. P.; Abruna, H. D. *Anal. Chem.* **1990,** *62,* 782-784.
14. Sabatani, E.; Rubinstein, I. *J. Phys. Chem.* **1987,** *91,* 6663-6669.
15. Bond, A. M.; Oldham, K. B.; Zoski, C. G. *Anal. Chim. Act.* **1989,** *216,* 177-230.
16. Smith, C. P.; White, H. S. *Anal. Chem.* **1993,** *65,* 3343-3353.

17. Penner, R. M.; Martin, C. R. *Anal. Chem.* **1987,** *59,* 2625-2630.

18. Cheng, I. F.; Martin, C. R. *Anal. Chem.* **1988**, 60, 2163-2165.

19. Cheng, I.F.; Whiteley, L. D.; Martin, C. R. Anal. Chem. **1989**, 61, 762-766.

20. Szentirmay, M. N.; Martin, C. R. *Anal. Chem.* **1984**, 56, 1898-1902.

21. Lindsay, J. K.; Hauser, C. R. *J. Org. Chem.* **1957,** *22,* 355-358.

22. Van de Poel, J.; Neuman, H.M. *Inorg. Synth.* **1968,** *11,* 53-56.

23. Fleischer, R. L.; Price, P. B.; Walker, R. M. *Nuclear Tracks in Solids, Principles and Applications,* **1975,** University of California Press, Berkeley, CA.

24. Amatore, C.; Savéant, J.M.; Tessier, D. *J. Electroanal. Chem.* **1983,** *147,* 39-51.

25. Gueshi, T.; Tokuda, K.; Matsuda, H. *J. Electroanal. Chem.* **1978,** *89,* 247-260.

26. Mallory, G. O.; Hajdu, J. B. (Eds.) *Electroless Plating: Fundamentals and Applications,* American Electroplaters and Surface Finishers Society, Orlando, FL, **1990,** Chap. 1, pp. 1-55.

27. Reference 24, Chap. 17, pp. 441-444..

28. Brumlik, C. J.; Menon, V. P.; Martin, C. R. *J. Mater. Res.* **1994,** *9,* 1174-1183.

29. Furness,R.W. *The practice of plating on plastics,* Robert Draper Ltd. Surrey, UK, **1968**, Chap. 8, pp. 41-42.

30. McDermott, J. *Plating of Plastics with Metals,* Noyes Data Corporation, Park Ridge, NJ, **1974**, pp. 181.

31. Foss, C. A.; Hornyak, G. L.; Stockert, J. A.; Martin, C. R. *J. Phys. Chem.* **1992,** *96,* 7497-7499.

32. Foss, C. A.; Hornyak, G. A.; Stockert, J. A.; Martin, C. R. *J. Phys. Chem.* **1994,** *98,* 2963-2971.

33. Nishizawa, M.; Menon, V.P.; Martin,C.R. *Science,* accepted for publication.

34. Van de Hulst, H. C. *Light Scattering by Small Particles,* Dover Publications, Inc, NY, **1981**, pg 397.

35. Martin, C.R. *Science*, **1994,** *266,* 1961-1966.

36. Wehmeyer, K. R.; Wightman, R. M. *J. Electroanal. Chem.* **1985,** *196,* 417-421.

37. Bilewicz, R.; Majda, M. *J. Am. Chem. Soc.* **1991,** *113,* 5464-5466.

38. Nicholson, R. S. *Anal. Chem,* **1965,** *37,* 1351-1355.

39. Menon,V.P.; Martin,C.R. In prep.

40. Ballarin,B.; Brumlik,C.J.; Lawson,D.R.; Liang,W.; Van Dyke,L.S.; Martin,C.R. *Anal. Chem.* **1992,** 64, 2647-2651.

41. White, H.S.; Bard, A.J.; Fan, F-R. Personal communication, July, 1994.

FIGURE CAPTIONS

1. Schematic diagram of the electroless procedure used to deposit gold in the pores of the polycarbonate template membrane.
2. Schematic diagram of the fabrication of the nanoelectrode ensembles (NEEs) .
3. A) Transmission electron micrograph of a microtomed section of a polycarbonate template membrane after deposition of Au tubules within the pores of the membrane. Pore diameter was 50-nm; plating time was 10 min. B) Scanning electron micrograph (SEM) of surface of a 30NEE. C) SEM of Au nanowires (50 nm diameter) obtained after dissolving away the polycarbonate template membrane. In B and C, the sample was sputtered with a thin (‹30 nm) layer of Au prior to imaging in order to eliminate surface charging.
4. UV-Vis spectra of a 30NEE and a 10NEE.
5. Cyclic voltammograms at 100 mV/s at a 10NEE in 5 μM aqueous $TMAFc^+$, 1 mM $NaNO_3$ A) Before thermal treatment and B) After thermal treatment of the NEE.
6. Background cyclic voltammograms in 50 mM sodium nitrate at 100 mV/s for - A) gold macro-disk electrode. B) 30NEE. C) 10NEE. The geometric area for all electrodes was 0.079 cm^2.
7. Simulated (dotted curves) and experimental (solid curves) voltammograms at 100 mV/s at a 10NEE (0.079 cm^2 geometric area) in 5 μM $TMAFc^+$ and 0.5 mM sodium nitrate. Simulation assumes the total overlap limiting case (i.e. a macro-electrode with area = 0.079 cm^2).
8. Cyclic voltammograms for 5 μM $Ru(NH_3)_6Cl_3$ and 10 mM pH 7 phosphate buffer as supporting electrolyte. A) 30NEE. B) 10NEE.

Scan rates are 20, 50 and 100 mV/s

9. Cyclic voltammograms at 100 mV/s in aqueous $TMAFc^+$ at A) A gold macro-disk electrode in 50 mM sodium nitrate. B) A 10NEE in 1 mM sodium nitrate. $TMAFc^+$ concentrations are as indicated; electrode geometric area in both cases=0.079 cm^2.

10. Plot of log(anodic peak current) from $TMAFc^+$ voltammograms vs. log([$TMAFc^+$]). A) Macro-disk electrode. B) 10NEE. Conditions as per Figure 10.

11. Cyclic voltammograms illustrating the effect of supporting electrolyte concentration at a 10NEE. 5 μM $TMAFc^+$ in aqueous $NaNO_3$ at the indicated concentrations of $NaNO_3$. Scan rate = 100 mV/s

Table I. Characteristics of the membranes used to prepare the NEEs

Pore diameter[a] (nm)	Pore density ($pores/cm^2$) [a]	Average center to center distance (nm) [b]	Fractional pore area [c]	Fractional electrode area [d]
30	6×10^8	200	0.0042	0.0045
10	6×10^8	200	0.00047	0.00094

[a] From Poretics Inc. product literature.

[b] Calculated from equation1 in reference 19.

[c] Calculated from nominal pore size and density.

[d] Obtained experimentally from double layer charging currents.

Table II. **ΔE_{pk} values as a function of scan rate for $Ru(NH_3)_6^{3+}$ cyclic voltammograms at a 30NEE and a 10NEE.**

Scan rate (mV/s)	ΔEpk (mV)	
	30NEE	10NEE
5	60	72
10	62	76
20	65	80
50	70	90
100	75	100

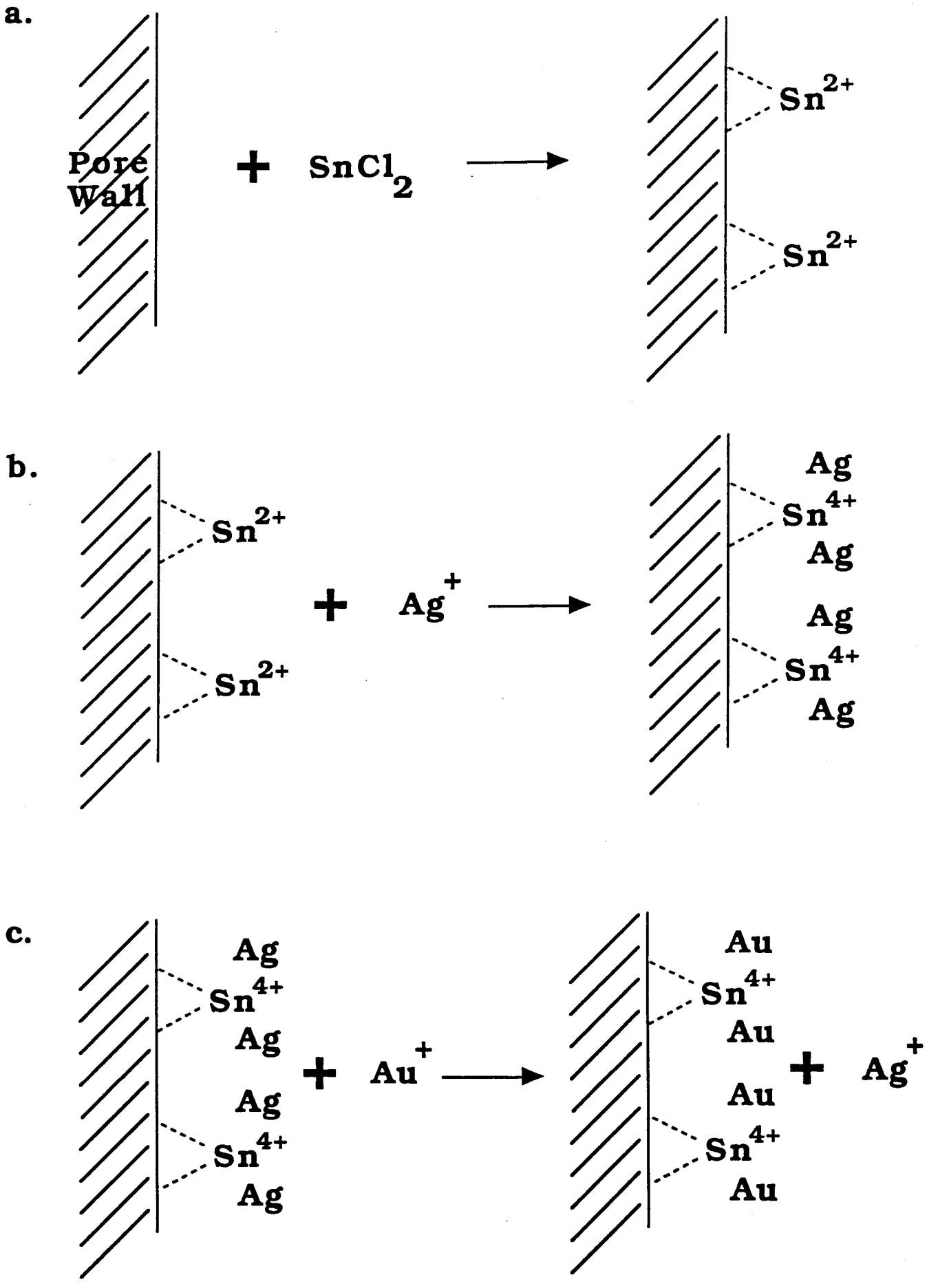
a.
Pore Wall
+ SnCl2
Sn2+
Sn2+
b.
Sn2+
Sn2+
+ Ag+
Ag
Sn4+
Ag
Ag
Sn4+
Ag
c.
Ag
Sn4+
Ag
Ag
Sn4+
Ag
+ Au+
Au
Sn4+
Au
Au
Sn4+
Au
+ Ag+

FIGURE 1

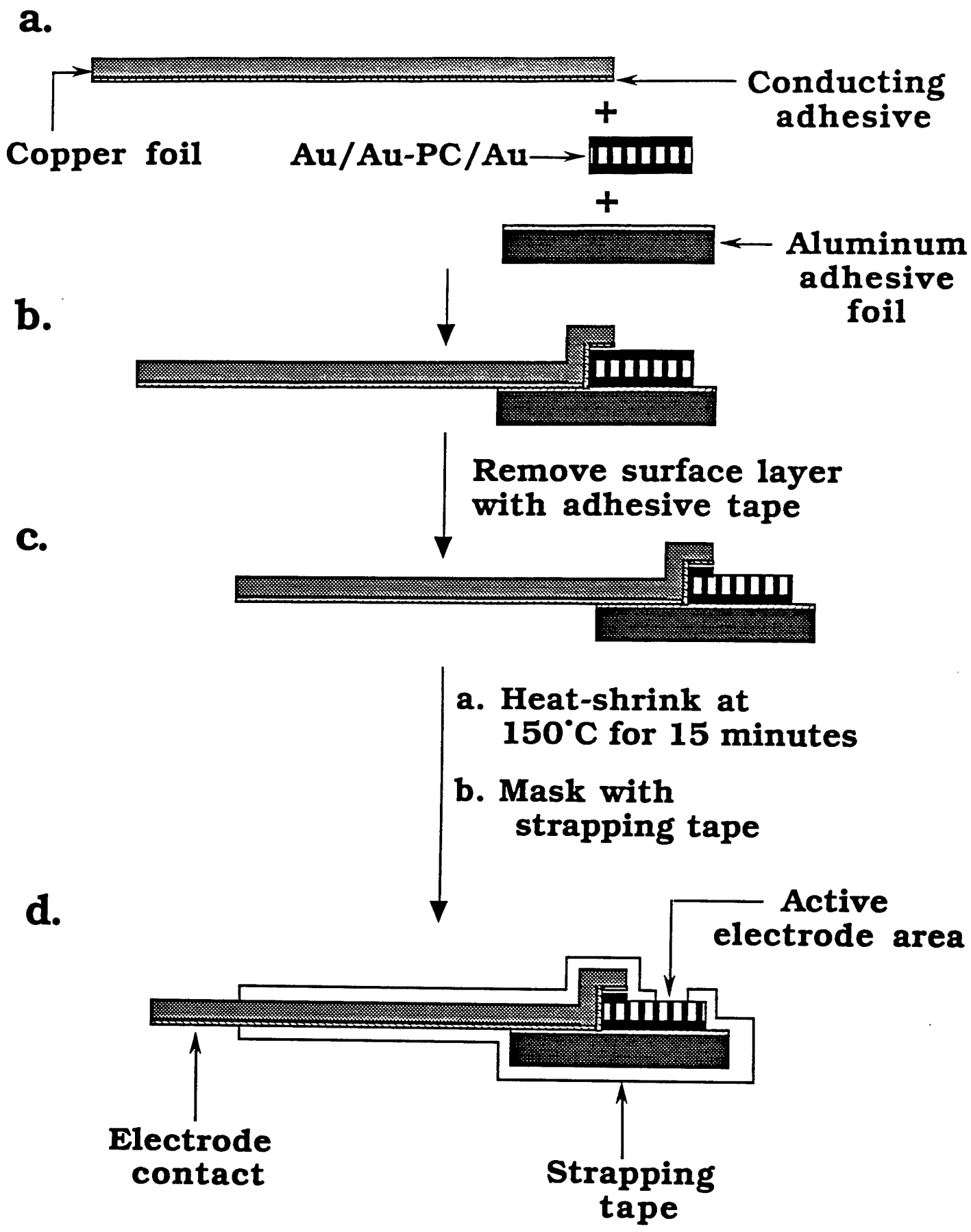
a.
Conducting adhesive
+
Copper foil
Au/Au-PC/Au
+
Aluminum adhesive foil
b.
Remove surface layer with adhesive tape
c.
a. Heat-shrink at 150°C for 15 minutes
b. Mask with strapping tape
d.
Active electrode area
Electrode contact
Strapping tape

FIGURE 2

FIGURE 3A

B

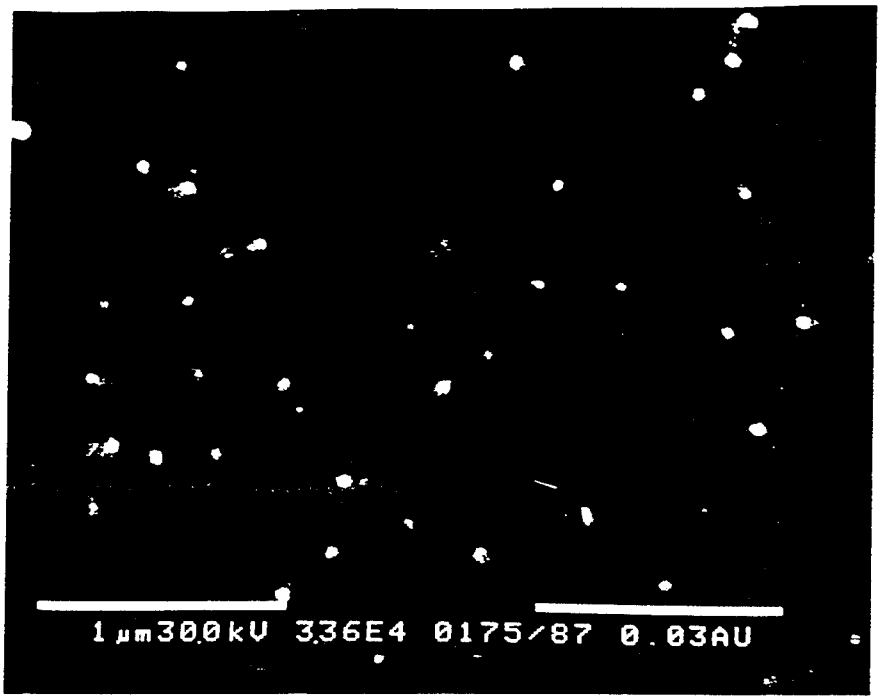

C

FIGURE 3B & C

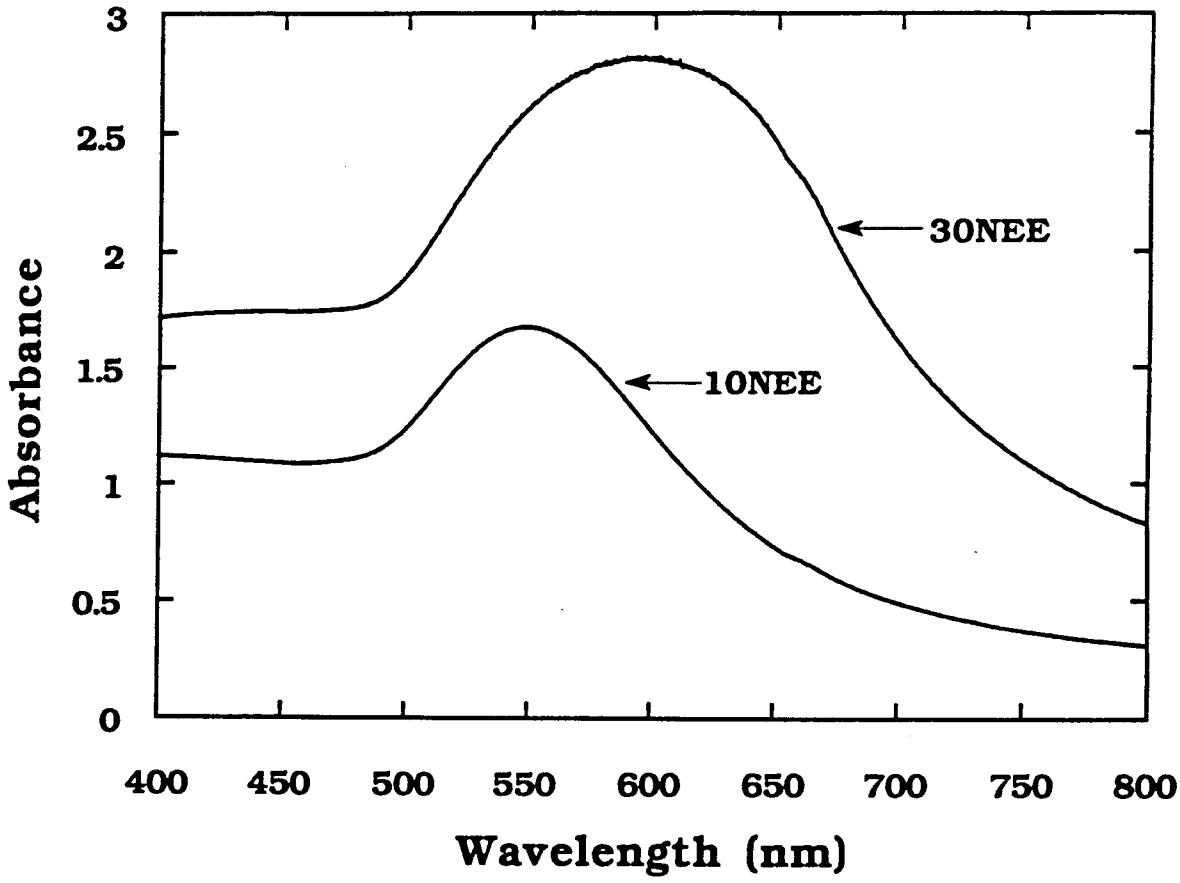
3
2.5
2
1.5
1
0.5
0
Absorbance
30NEE
10NEE
400
450
500
550
600
650
700
750
800
Wavelength (nm)

FIGURE 4

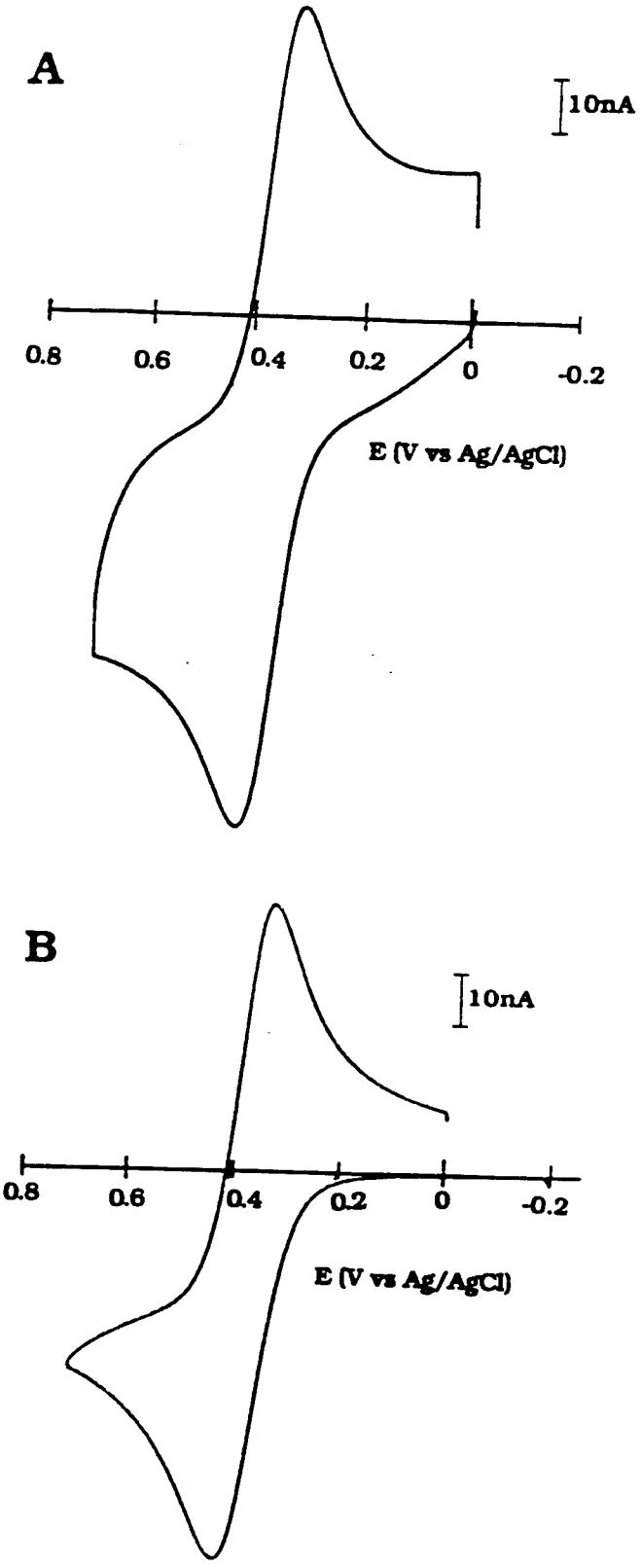
A
10nA
0.8
0.6
0.4
0.2
0
-0.2
E (V vs Ag/AgCl)
B
10nA
0.8
0.6
0.4
0.2
0
-0.2
E (V vs Ag/AgCl)

FIGURE 5

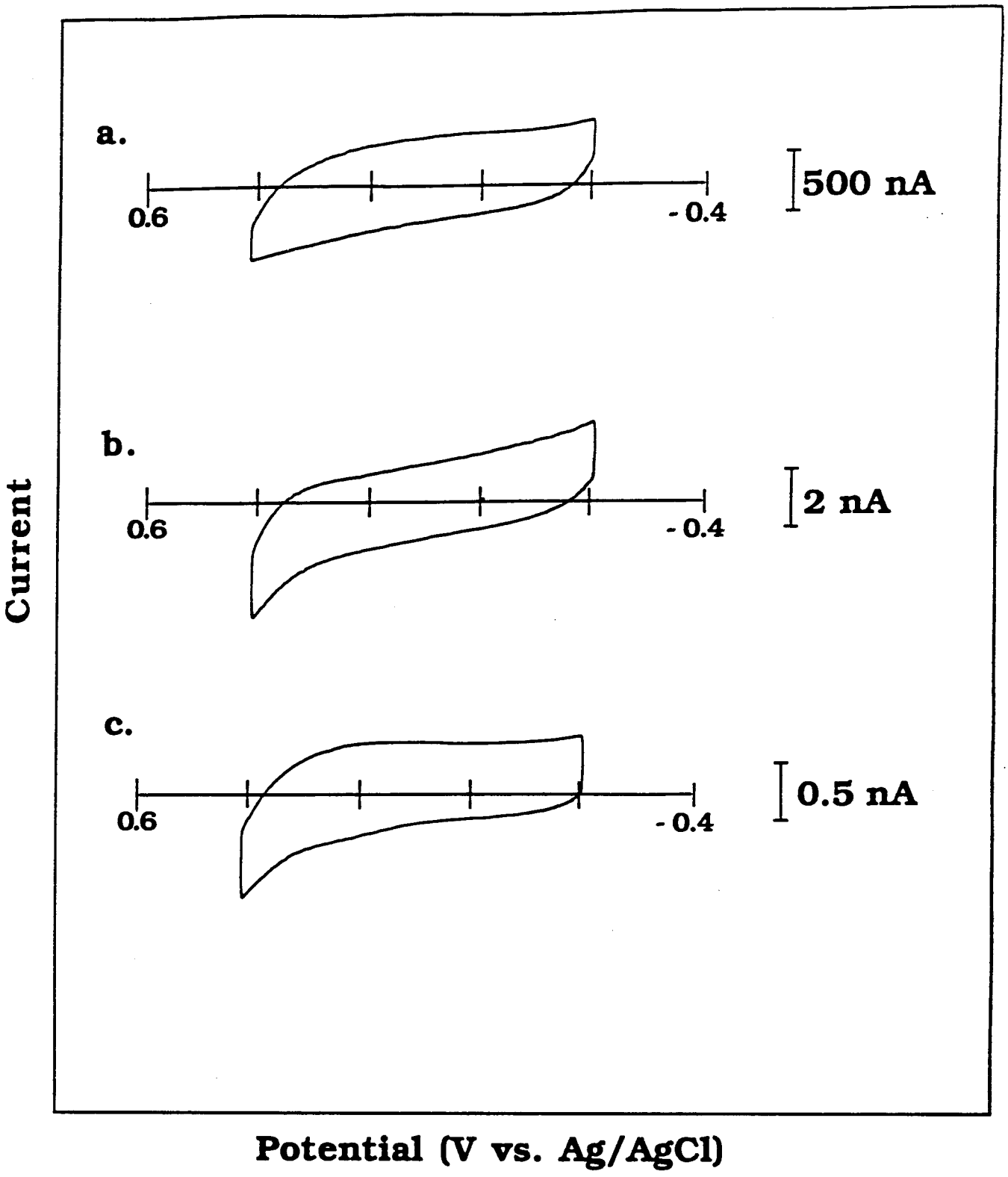
a.
0.6
- 0.4
500 nA
b.
0.6
- 0.4
2 nA
c.
0.6
- 0.4
0.5 nA
Current
Potential (V vs. Ag/AgCl)

FIGURE 6

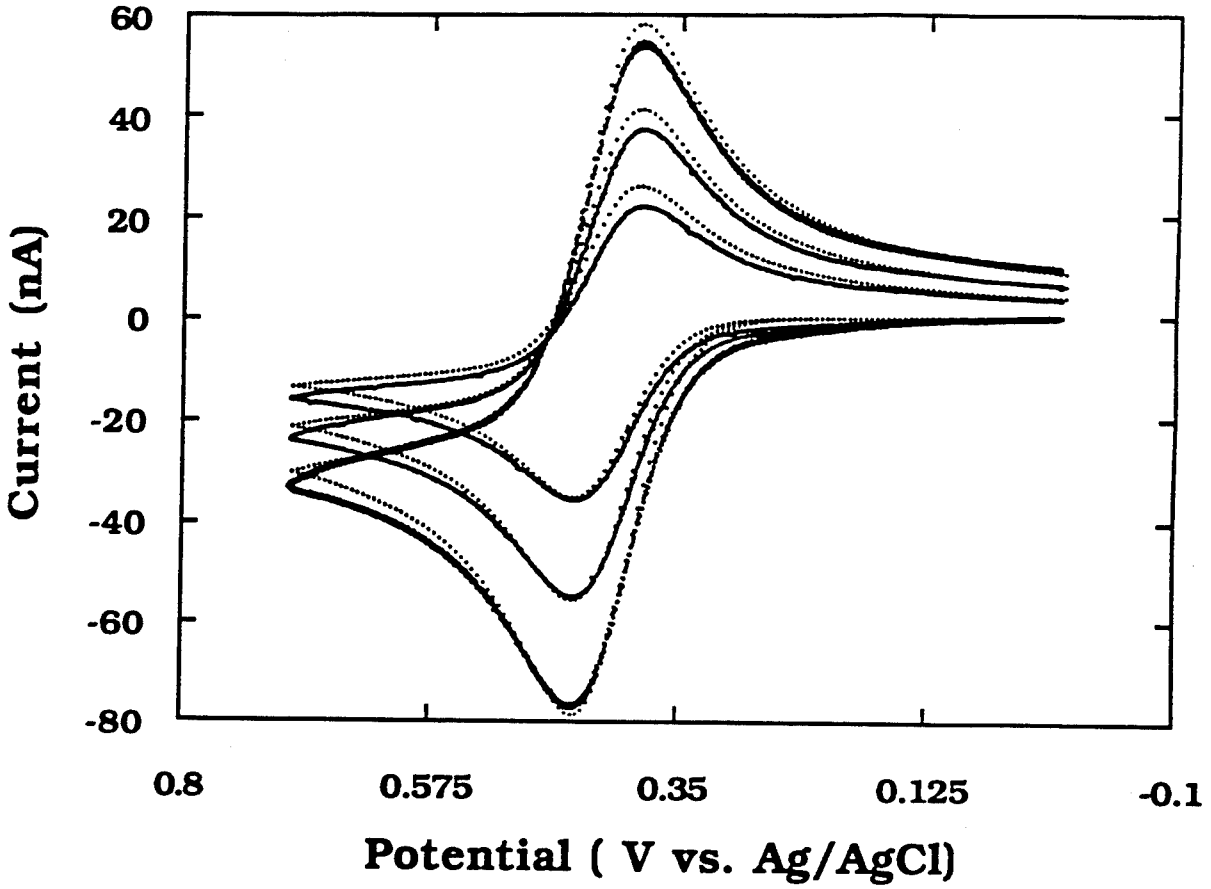
60
40
20
0
-20
-40
-60
-80
Current (nA)
0.8
0.575
0.35
0.125
-0.1
Potential (V vs. Ag/AgCl)

FIGURE 7

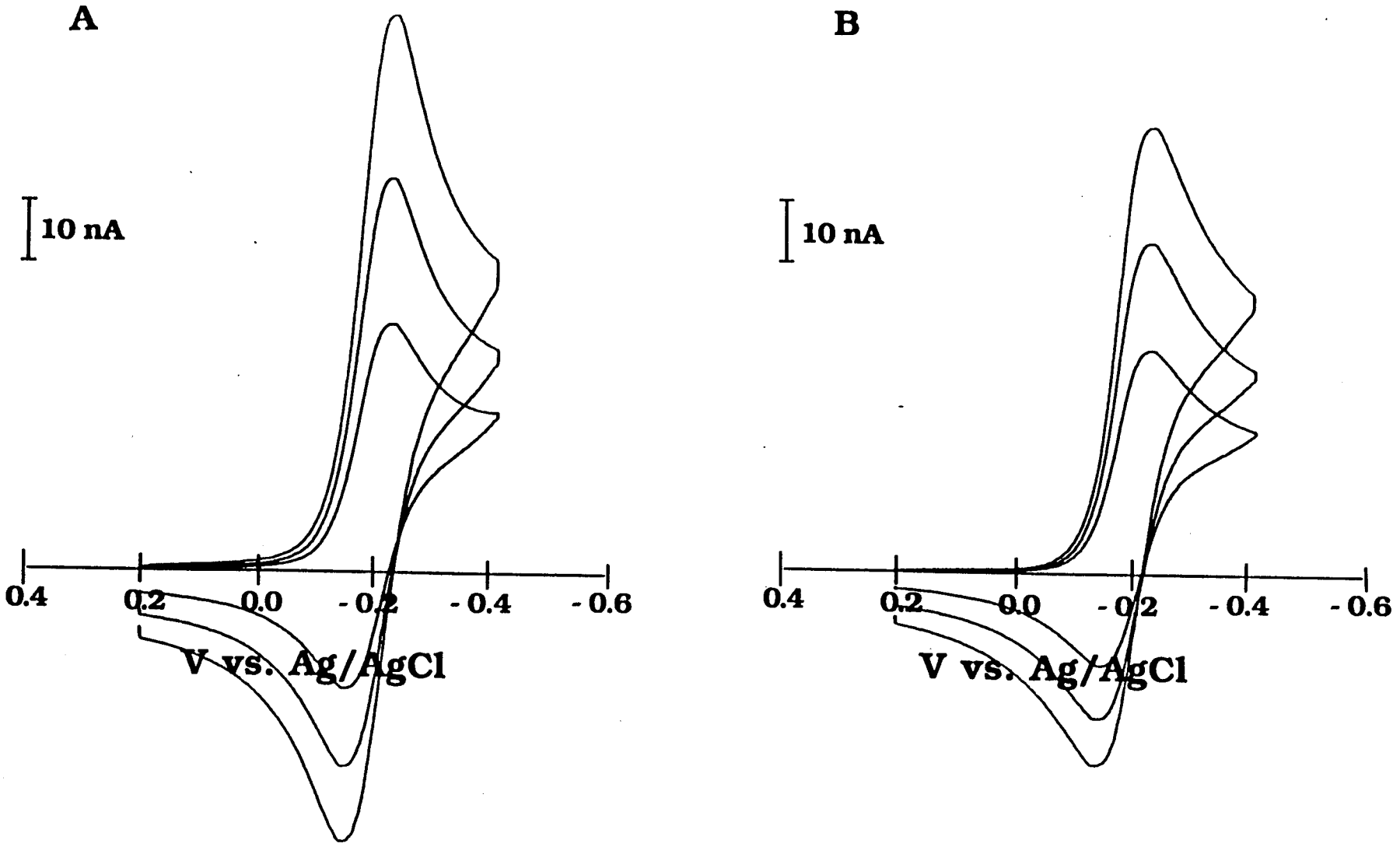
A
10 nA
0.4
0.2
0.0
- 0.2
- 0.4
- 0.6
V vs. Ag/AgCl
B
10 nA
0.4
0.2
0.0
- 0.2
- 0.4
- 0.6
V vs. Ag/AgCl

FIGURE 8

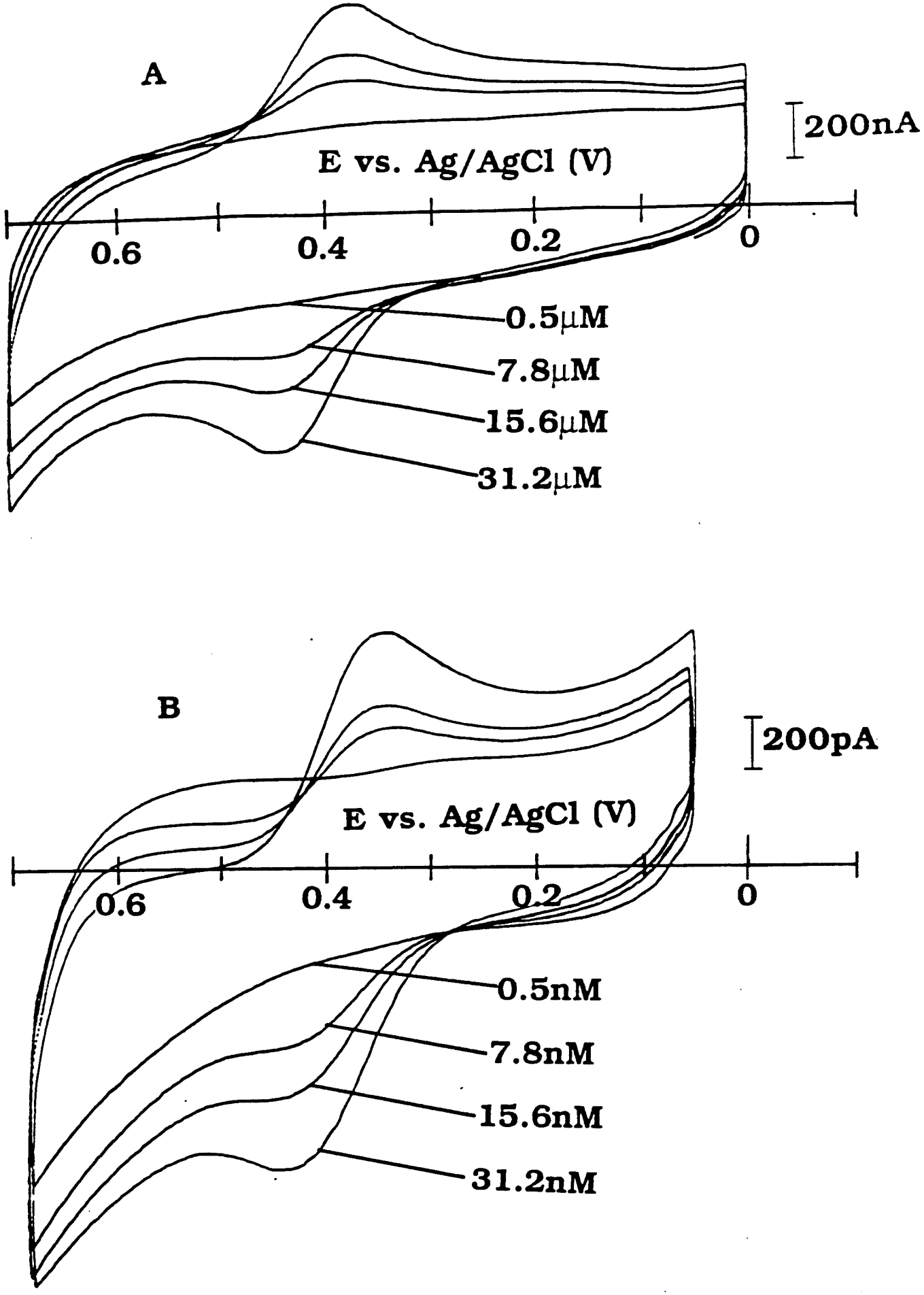
A
200nA
E vs. Ag/AgCl (V)
0.6
0.4
0.2
0
0.5μM
7.8μM
15.6μM
31.2μM
B
200pA
E vs. Ag/AgCl (V)
0.6
0.4
0.2
0
0.5nM
7.8nM
15.6nM
31.2nM

FIGURE 9

A

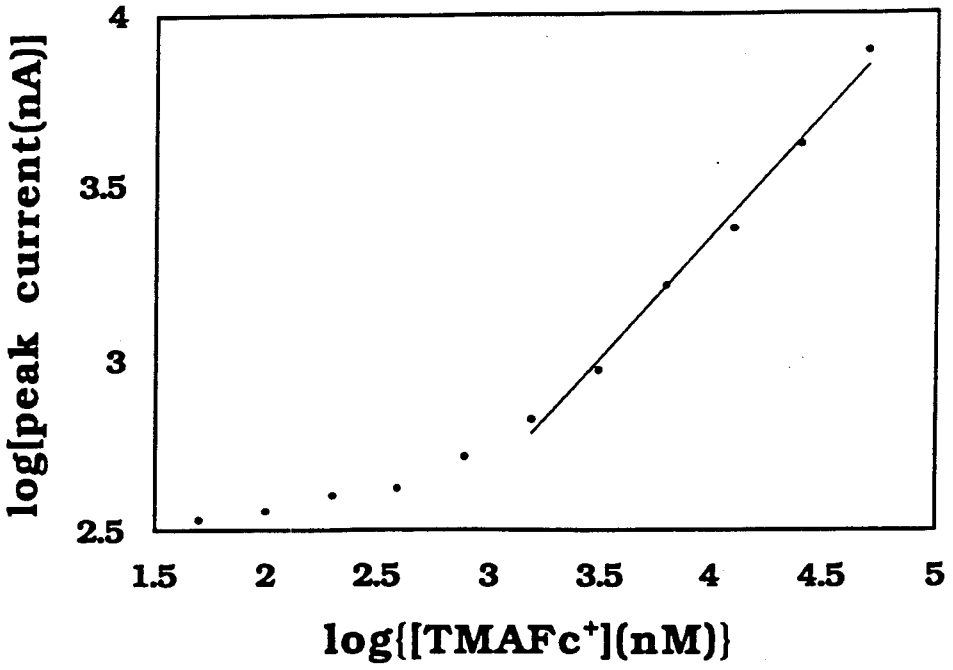
log[peak current(nA)]
4
3.5
3
2.5
1.5
2
2.5
3
3.5
4
4.5
5
log{[TMAFc+](nM)}

B

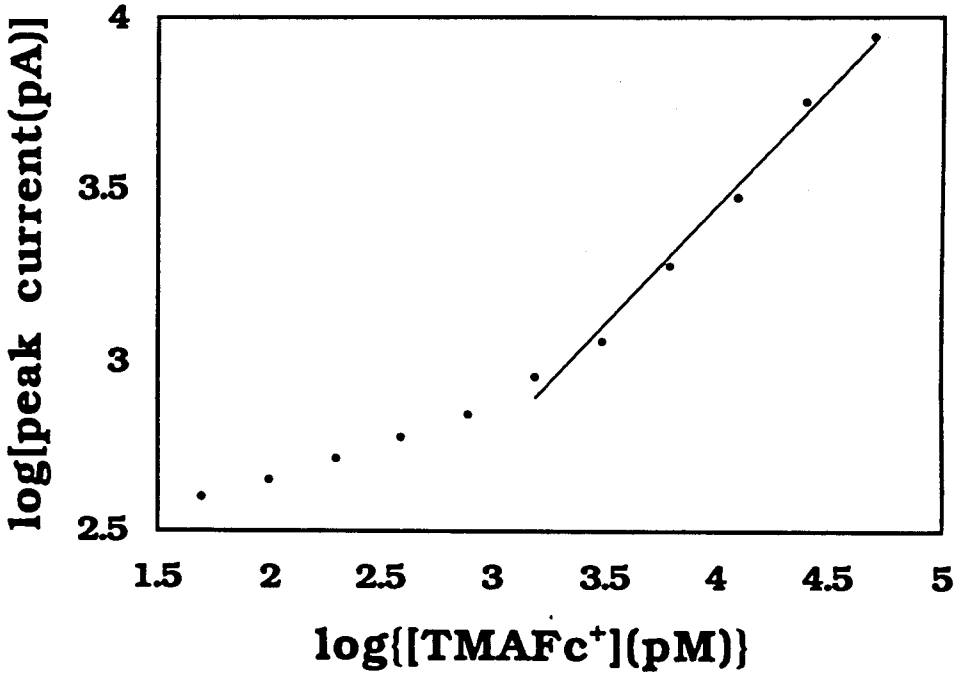
log[peak current(pA)]
4
3.5
3
2.5
1.5
2
2.5
3
3.5
4
4.5
5
log{[TMAFc+](pM)}

FIGURE 10

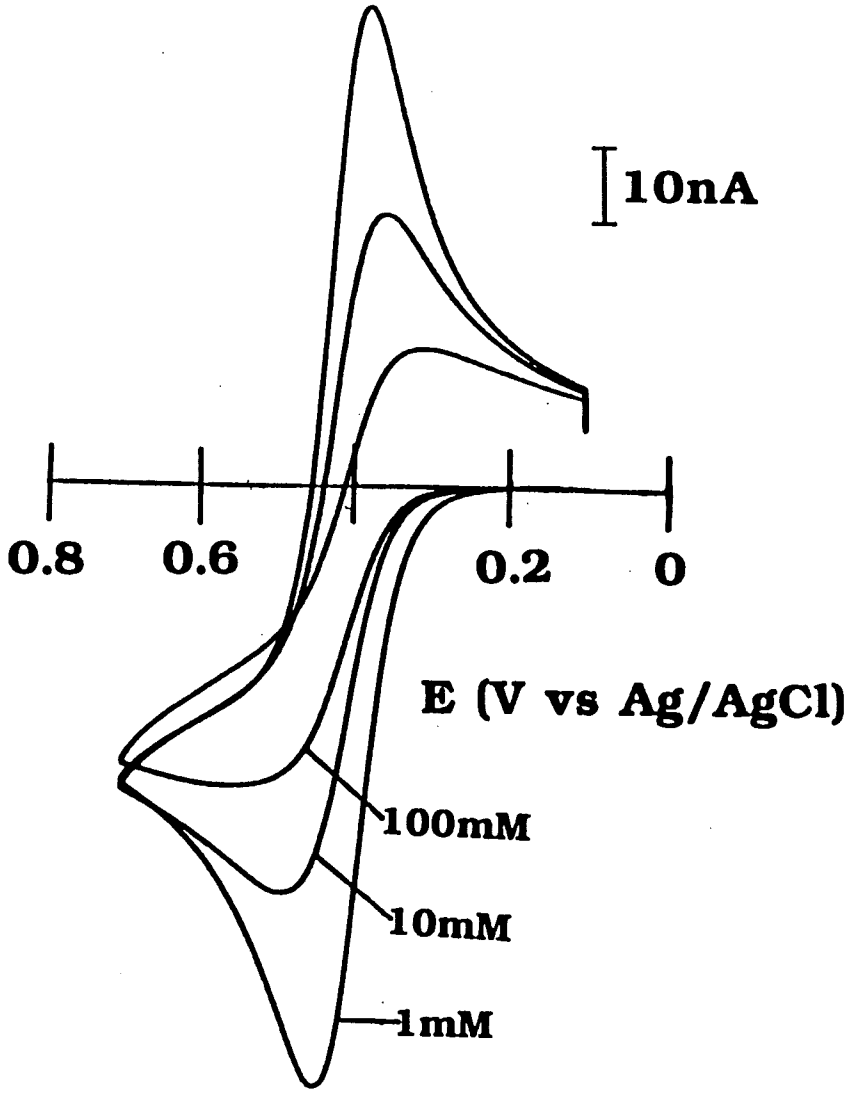

FIGURE 11